Separation and Purification Technology 301 (2022) 121965

Contents lists available at ScienceDirect

Separation and Purification Technology

journal homepage: www.elsevier.com/locate/seppur

Magnetic $MgFe_2O_4$/MIL-88A catalyst for photo-Fenton sulfamethoxazole decomposition under visible light

Ke-Xin Shi [a], Fuguo Qiu [a,b], Peng Wang [a], Haiyan Li [b,c], Chong-Chen Wang [a,b,c,*]

[a] Beijing Key Laboratory of Functional Materials for Building Structure and Environment Remediation, School of Environment and Energy Engineering, Beijing University of Civil Engineering and Architecture, Beijing 100044, China

[b] Beijing Energy Conservation & Sustainable Urban and Rural Development Provincial and Ministry Co-construction Collaboration Innovation Center, Beijing University of Civil Engineering and Architecture, Beijing 100044, China

[c] Beijing Engineering Research Center of Sustainable Urban Sewage System Construction and Risk Control, Beijing University of Civil Engineering and Architecture, Beijing 100044, China

ARTICLE INFO

Keywords:
MIL-88A
$MgFe_2O_4$
Photo-Fenton
Sulfamethoxazole
Oxidation

ABSTRACT

Series magnetic $MgFe_2O_4$/MIL-88A catalysts (MFxMy) were fabricated by a simple ball-milling method, which were applied to degrade sulfamethoxazole (SMX) antibiotic via photo-Fenton process under low power visible light. The influences of initial pH, H_2O_2 concentration, and co-existing inorganic anions on SMX degradation were explored. The results revealed that the optimal $MgFe_2O_4$/MIL-88A (MF140M60) demonstrated excellent photo-Fenton catalysis activity, in which ca. 99.8% of SMX could be degraded within 20.0 min. The outstanding catalytic activity of $MgFe_2O_4$/MIL-88A (MF140M60) can be ascribed to the effective transfer of charge carriers between $MgFe_2O_4$ and MIL-88A. As well, the optimal $MgFe_2O_4$/MIL-88A (MF140M60) catalyst possessed good stability and recyclability.

1. Introduction

The sulfamethoxazole (SMX), as emerging pharmaceutical, attracted increasing concerns considering their potential risk to the ecosystem and human beings [1–4]. Long term exposure to SMX in aquatic environment might induce the antibiotic resistant bacteria (ARBs) and even antibiotic resistance genes (ARGs), which exerted huge pressure to humankind [5]. In addition, the synergistic effect of sulfamethoxazole with other pharmaceuticals inhibited the growth of human embryonic cells [6]. Therefore, it is a necessity to develop treatment strategies for the removal of SMX.

To date, a variety of technologies were used for SMX degradation, such as biodegradation [7], adsorption [8], membrane filtration [9] and advanced oxidation process (AOPs) [10]. Among these technologies, AOPs as efficient, rapid and simple technologies have been widely adopted to water treatment owing to its advantages over other technologies [11–13]. As one of the AOPs strategies, the heterogeneous photo-Fenton oxidation is an excellent technology to remove stable pollutants from polluted water because it can overcome the drawbacks of homogeneous Fenton oxidation, in which has attracted widespread attention [14–16].

In the past decades, metal–organic frameworks (MOFs) have been proved to be promising materials because of their ultra-high specific surface areas, tunable pore sizes, open crystalline frameworks [17–19]. MOFs can also be used as heterogeneous catalysts in photo-Fenton process [12,20]. Especially, Fe-based MOFs exhibit great potential as heterogeneous photocatalysts because of their Fe-O clusters, which can lead to a photo-Fenton reaction under light irradiation [21,22]. In addition, Fe element exhibited low toxicity and eco-friendly [23]. Among various Fe-based MOFs, MIL-88A has attracted increasing interest in water treatment via photo-Fenton reactions due to facile synthesis and high throughput production [24,25]. Fu et al. [24] prepared MIL-88A at room temperature, which was green and conductive to the large-scale synthesis. Chen et al. [26] constructed PANI/MIL-88A(Fe) by one-pot hydrothermal method to reduce Cr(VI) and achieved efficient photo-Fenton degradation of pollution.

Combining MOFs with magnetic materials can not only improve degradation performance, but also facilitate recovery with the aid of external magnetic fields [27]. To date, several magnetic materials have been tested for wastewater treatment, such as magnetite (Fe_3O_4),

* Corresponding author at: Beijing Key Laboratory of Functional Materials for Building Structure and Environment Remediation, School of Environment and Energy Engineering, Beijing University of Civil Engineering and Architecture, Beijing 100044, China.
E-mail address: wangchongchen@bucea.edu.cn (C.-C. Wang).

https://doi.org/10.1016/j.seppur.2022.121965
Received 24 June 2022; Received in revised form 16 August 2022; Accepted 17 August 2022
Available online 20 August 2022

maghemite (γ-Fe_2O_3), spinel ferrite (MFe_2O_4), hexaferrite ($MFe_{12}O_{19}$) and orthoferrite ($MFeO_3$) [28–31]. Gu et al. synthesized magnetic MIL-88A/BiOBr/$SrFe_{12}O_{19}$ to degrade Rhodamine B (RhB) and methylene blue (MB), in which the enhanced photocatalytic performance can be ascribed to the formation of dual Z-scheme heterojunction [32]. Among all magnetic materials, magnesium ferrite ($MgFe_2O_4$) as a spinel ferrite, has attracted considerable attentions because of moderate saturation magnetization, high chemical stability and contains no toxic heavy metal ions [33,34].

Within this paper, the magnetic $MgFe_2O_4$/MIL-88A composite catalysts were prepared by ball-milling method to achieve the SMX degradation via photo-Fenton reaction. Furthermore, investigation of the effects of key environmental factors and the degradation mechanism on SMX degradation were carried out. The results showed the as-obtained $MgFe_2O_4$/MIL-88A catalysts (MF*x*M*y*) exhibited excellent stability and reusability, which was easy to practically accomplish catalysts recovery in wastewater treatment.

2. Experimental

The chemicals, the characterization instruments and the corresponding methods were described in the Supplementary Information (SI).

2.1. Preparation of catalysts

MIL-88A and $MgFe_2O_4$ were synthesized according to the previous literatures with slight modifications [26,35]. The information of preparation details was provided in the Supplementary Information.

$MgFe_2O_4$/MIL-88A (MF*x*M*y*) composites were fabricated by ball-milling treatment under 30 Hz for 20 min toward the mixture of as-prepared $MgFe_2O_4$ and MIL-88A with specific mass ratios (The letters "MF" and "M" represent $MgFe_2O_4$ and MIL-88A, respectively. The "*x*" and "*y*" are the mass fraction of $MgFe_2O_4$ and MIL-88A, respectively).

2.2. Performance test

All the SMX degradation experiments were carried out in an aqueous solution containing 50.0 mL of SMX (5.0 mg/L) at room temperature with a certain amount of catalyst. The pH values of the solution were adjusted by H_2SO_4 (0.1 mM) or NaOH (0.1 mM) solutions. After being stirred for 30.0 min in dark to accomplish adsorption–desorption equilibrium, a certain amount of H_2O_2 was added to the solution under visible light (350 mW low power LED light, PCX50C, Beijing Perfectlight Technology Co., Ltd.) to initiate the degradation process. Additionally, 1.0 mL of the reaction solution was collected and filtered by a 0.22 μm springe at 5.0 min intervals, in which 0.01 mL of isopropanol was added to quench the reaction immediately. The concentrations of residual SMX was determined by liquid chromatography (LC-20A, Shimadzu, Japan), which was equipped with a UV–Vis detector which was set as 270 nm and Eclipse Plus C18 column (250 mm × 2.1 mm , 5 μm). The mobile phase is the matrix of acetonitrile and 0.1% phosphoric acid (45/55, *v*/*v*) with the flow rate of 0.80 mL min^{-1}. The other information was listed in Supplementary Information.

3. Results and discussion

3.1. Characterizations

The crystalline phases of as-prepared $MgFe_2O_4$, MIL-88A, and MF*x*M*y* were ascertained by the powder X-rat diffraction (PXRD) as depicted in Fig. 1a. The typical peaks for $MgFe_2O_4$ could be observed at 2θ of 30.1° (220), 35.4° (311), 43.0° (400), 53.4° (422), 56.9° (511), and 62.5° (440), which complied with the standard one (PDF#97-000-9939). Additionally, the PXRD patterns of MIL-88A(Fe) matched perfectly with those reported literature [36] and the standard PXRD patterns (Fig. S1). As for $MgFe_2O_4$/MIL-88A composites, the main peaks accorded well with both pure $MgFe_2O_4$ and MIL-88A. With the increasing content of $MgFe_2O_4$, the characteristic peaks of $MgFe_2O_4$ strengthen, while the diffraction peaks of MIL-88A(Fe) weaken. It's mainly due to the mask of $MgFe_2O_4$ and relatively low diffraction intensity of MIL-88A [37]. According to the results, the $MgFe_2O_4$/MIL-88A composites were successfully prepared.

The characteristic functional groups of as-prepared materials were proofed by fourier transform infrared (FTIR) study (Fig. 1b). For $MgFe_2O_4$/MIL-88A composites, the characteristic peaks at 1396.8 cm^{-1} and 1600.9 cm^{-1} were ascribed to the symmetric and asymmetric vibration of —COOH [38,39]. The bending vibration of C—H and the stretching vibration of C—C in MIL-88A were located at 980.4 cm^{-1} and 1218.7 cm^{-1}, respectively [39]. In addition, the absorption peaks at 442 cm^{-1} and 587.8 cm^{-1} were assigned to Mg—O and Fe—O stretching in $MgFe_2O_4$, respectively [40]. Thus, the PXRD and FTIR confirmed the successful combination of $MgFe_2O_4$ and MIL-88A.

The scanning electron microscopy (SEM) and transmission electron microscopy (TEM) images of the pure $MgFe_2O_4$, MIL-88A(Fe), and MF140M60 displayed the detailed morphological features (Fig. 2). It was observed that $MgFe_2O_4$ possess a typical spherical structure with diameters ranging from 100 nm to 200 nm (Fig. 2a and d). The as-prepared MIL-88A(Fe) displayed the well-crystallized fusiform morphology with a diameter of 200 nm and a length of 1.0–1.5 μm (Fig. 2b and e),which was comparable to that reported in previous literature [36]. The SEM and TEM images of MF140M60 in Fig. 2c and f revealed the edges and corners of the MIL-88A still maintained the original morphology, in which the $MgFe_2O_4$ particles were attached to the surface of MIL-88A tightly and evenly to form the heterostructures. The high-resolution transmission electron microscope (HRTEM) image

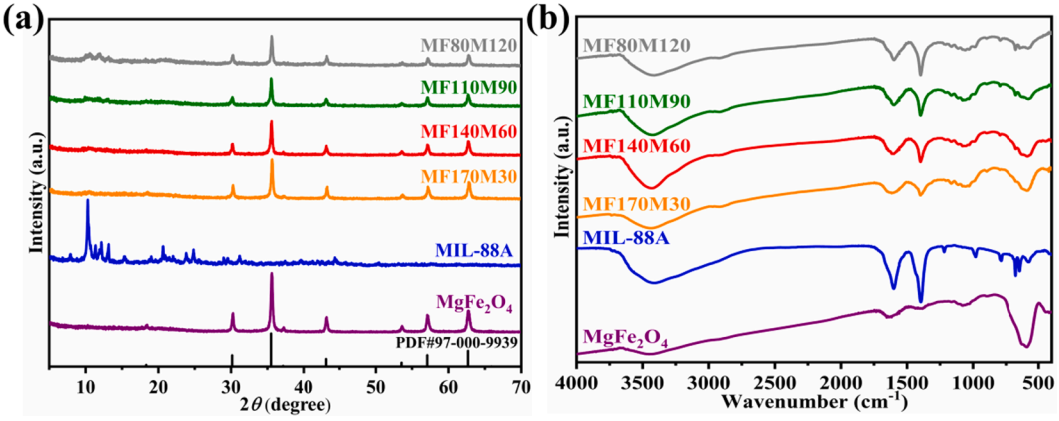

Fig. 1. (a) The PXRD patterns and (b) FTIR spectra of the different as-synthesized materials.

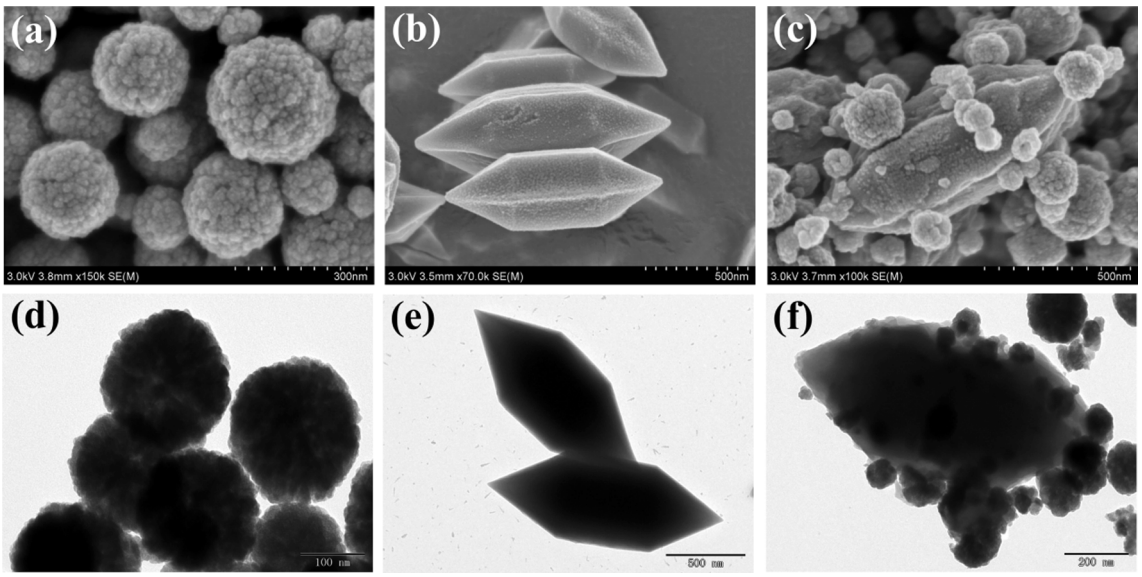

Fig. 2. The SEM and TEM images of (a, d) $MgFe_2O_4$, (b, e) MIL-88A and (c, f) MF140M60 composite.

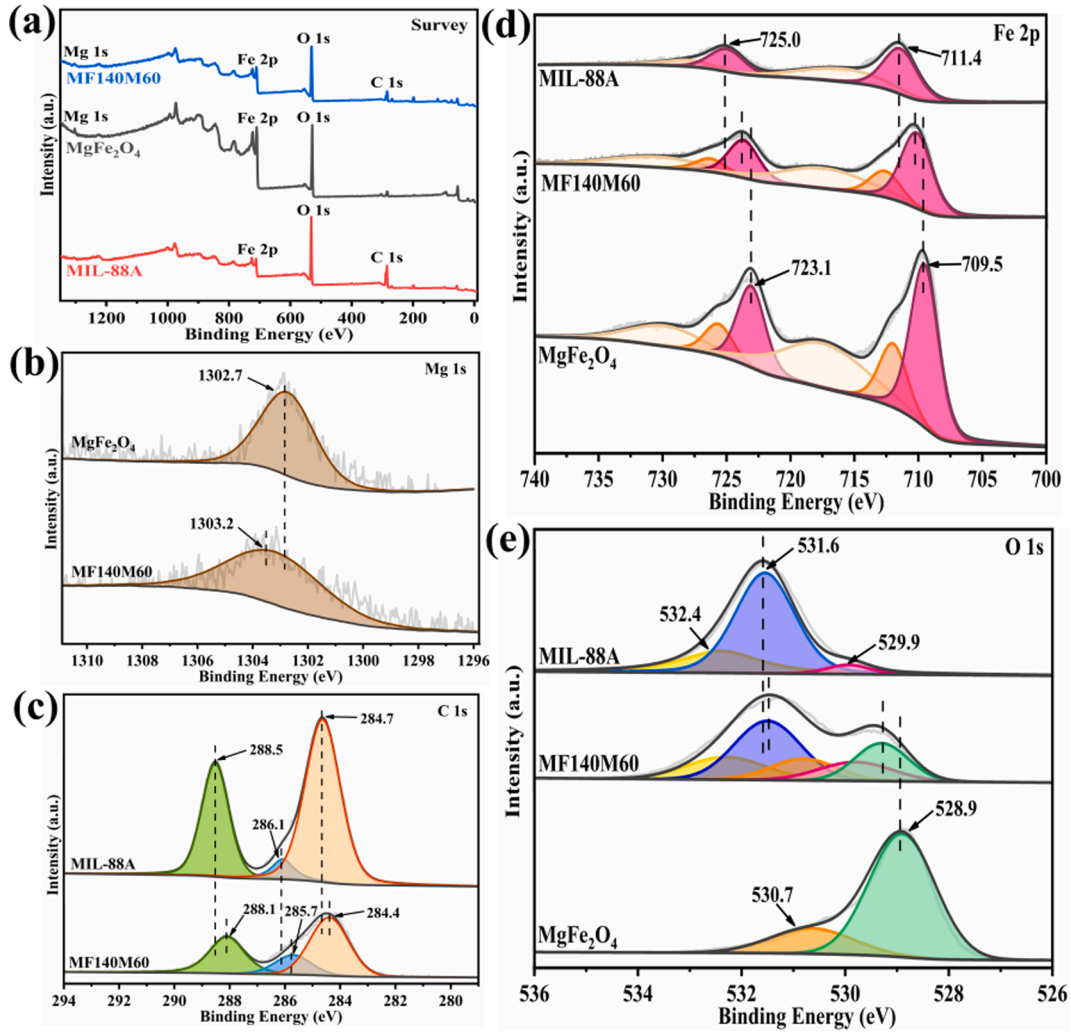

Fig. 3. (a) The XPS survey spectra and the high-resolution XPS spectra of (b) Mg 1s, (c) C 1s, (d) Fe 2p and (e) O 1s for $MgFe_2O_4$, MIL-88A and MF140M60.

of MF140M60 (Fig. S2) showed that the interface between $MgFe_2O_4$ and MIL-88A was distinct and tight, in which the spacing of 0.21 nm could be ascribed to the (4 0 0) facets of $MgFe_2O_4$ (PDF#97-000-9939), indicating the successful combination between $MgFe_2O_4$ and MIL-88A. Furthermore, the EDS elements mappings of MF140M60 was displayed in Fig. S3, in which the Mg, O, Fe and C elements could be observed. These findings affirmed that $MgFe_2O_4$ was grown on the surface of MIL-88A, in which the formed contact interfaces might facilitate the transfer of the charges transferred [41].

To further verify the surface elemental compositions and detailed chemical states of the as-prepared catalysts, the X-ray photoelectron spectroscopy (XPS) analysis was conducted. The coexistence of Fe 2p, Mg 1s, O 1s and C 1s in MF140M60 composite (Fig. 3a) matched well with the EDS elements mappings results. After being composited with $MgFe_2O_4$ by ball-milling, it could be found that the Mg 1s peaks were shifted from 1302.7 eV in $MgFe_2O_4$ to 1303.2 eV in MF140M60 (Fig. 3b). While the peaks of C 1 s at 284.7 eV, 286.1 eV and 288.5 eV in MIL-88A [42] were shifted to 284.4 eV, 285.7 eV and 288.1 eV in MF140M60, respectively (Fig. 3c). In the Fe 2p XPS spectrum of MIL-88A (Fig. 3d), the two peaks located at ca. 711.4 eV and 725.0 eV could be ascribed to the Fe $2p_{3/2}$ and Fe $2p_{1/2}$ [36]. For $MgFe_2O_4$, the Fe 2p could be split into tetrahedral Fe^{3+} (717.4 eV and 725.6 eV) and octahedral Fe^{3+} (709.5 eV and 723.1 eV) [43]. In the XPS spectrum of O 1 s (Fig. 3e), the peaks at 529.9 eV, 531.6 eV and 532.4 eV in MIL-88A were attributed to the carboxylate groups, lattice O^{2-} and H—O—H bonds, respectively [44]. The peaks at 528.9 eV and 530.7 eV for $MgFe_2O_4$ were ascribed to the Fe—O and Mg—O in spinel structure, respectively [45]. The peaks of Fe and O for MF140M60 shifted towards the binding energy between $MgFe_2O_4$ and MIL-88A. The phenomenon implied that the electrons might be transferred from $MgFe_2O_4$ to MIL-88A [46].

To better understand the catalytic performance of photo-Fenton catalysts, the optical properties of catalysts were further investigated by the UV–Vis diffuse reflectance spectra (UV–Vis DRS). As illustrated in Fig. 4a, the absorption region of pure $MgFe_2O_4$ included ultraviolet and visible regions. The composites presented wider and stronger absorption intensity in the visible region than the pure MIL-88A, due to the contribution of black $MgFe_2O_4$.

Furthermore, the optical bandgap energy of the as-prepared samples could be calculated. As illustrated in Fig. 4b, the E_g of pure MIL-88A and $MgFe_2O_4$ were ca. 2.75 eV and 1.72 eV, respectively, which were consistent with previous reports [36,47]. The reduction E_g value of MF*x*M*y* compared to pure materials can be attributed to the formed heterojunction between $MgFe_2O_4$ and MIL-88A, which could accomplish both the enhanced optical absorption capability and the reduced charge carriers recombination rate [48]. This phenomenon indicated that $MgFe_2O_4$ contributed greatly to the enhancement of visible light absorption.

3.2. Photo-Fenton activity of $MgFe_2O_4$/MIL-88A composites

Experimental results showed that the adsorbed SMX amounts on different catalysts could be neglected (<10%). In Fig. 5a, with the presence of H_2O_2, only 7.7% and 56.5% SMX were degraded in the presence of pure $MgFe_2O_4$ and MIL-88A, respectively. However, all the MF*x*M*y* composites showed quick and effective SMX degradation activities, which can be contributed to the synergistic interaction between $MgFe_2O_4$ and MIL-88A. The similar synergistic effects between the two materials were widely reported in previous works [27,32,49]. It was noteworthy that the $MgFe_2O_4$ + MIL-88A referred to the physical mixture of $MgFe_2O_4$ and MIL-88A under the optimal proportion without ball-milling. The $MgFe_2O_4$ + MIL-88A exhibited weaker degradation efficiency of SMX than the MF*x*M*y*, further demonstrating that the formation of heterojunction was formed in the MF*x*M*y* with the aid of the ball-milling treatment. Furthermore, when the mass proportion of the $MgFe_2O_4$/MIL-88A decreased from 170/30 to 140/60, a slight improvement in degradation performance occurred with SMX degradation efficiencies from 92.7% of MF170M30 to 96.8% of MF140M60 in 20 min. On the contrary, decline was observed for the SMX degradation efficiencies from 96.8% of MF140M60 to 81.2% of MF80M120 within 20 min. The photo-Fenton SMX degradation performances could be quantitatively compared via the degradation rate constants obtained from the quasi-first-order kinetic Langmuir-Hinshelwood mode (Fig. 5b). Correspondingly, the apparent reaction rate (k) of the SMX degradation reaction for MF140M60 was found to be 0.1533 min^{-1}, which was 117.9-folds and 7.8-folds higher than those of $MgFe_2O_4$ (0.0013 min^{-1}) and MIL-88A (0.0197 min^{-1}), respectively. Accordingly, the optimal MF140M60 for degrading SMX with the highest catalytic activity was selected to investigate the following experiments.

The SMX removal efficiencies in different catalytic reaction systems were shown in Fig. 5c. The results showed that the individual existence of H_2O_2, light and catalyst cannot degrade SMX effectively. Also, the photo activated H_2O_2 process (H_2O_2/light), and photocatalysis process (MF140M60/light) exerted little effect on target degradation. The SMX decomposition efficiencies in MF140M60/H_2O_2 and MF140M60/H_2O_2/light systems were 79.2% and 100% within 40 min, demonstrating that the light could accelerate the degradation efficiency of SMX. The synergistic effect of MF140M60, H_2O_2 and visible light was affirmed by reaction kinetic fitted by pseudo-first-order kinetic in different systems (Fig. 5d).

Additionally, the MF140M60 exhibited apparent magnetic properties owing to the successful loading of $MgFe_2O_4$. The MF140M60 catalysts could be separated from the solution under the action of applied magnetic field within 120 s (insert Fig. 5c). Thus, the excellent magnetic

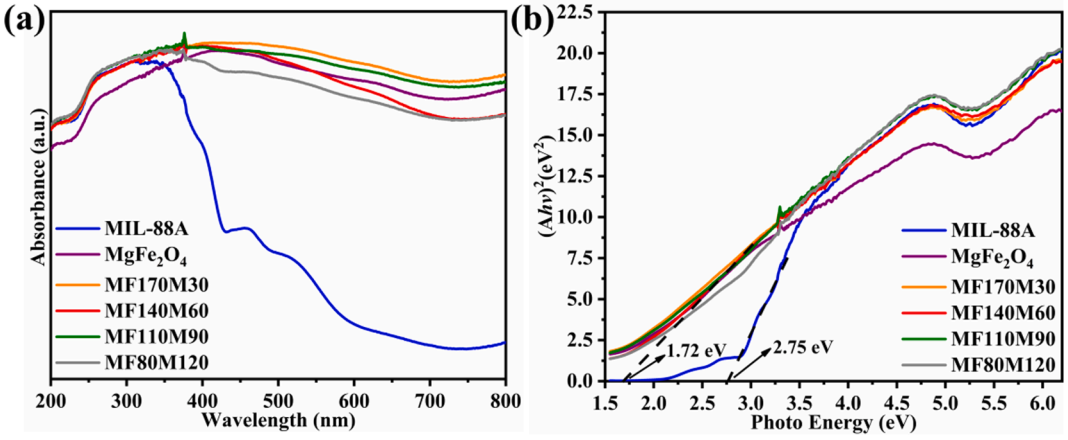

Fig. 4. (a) The UV–vis DRS spectra and (b) bandgap energies of MIL-88A (Fe), $MgFe_2O_4$ and MF*x*M*y* catalysts.

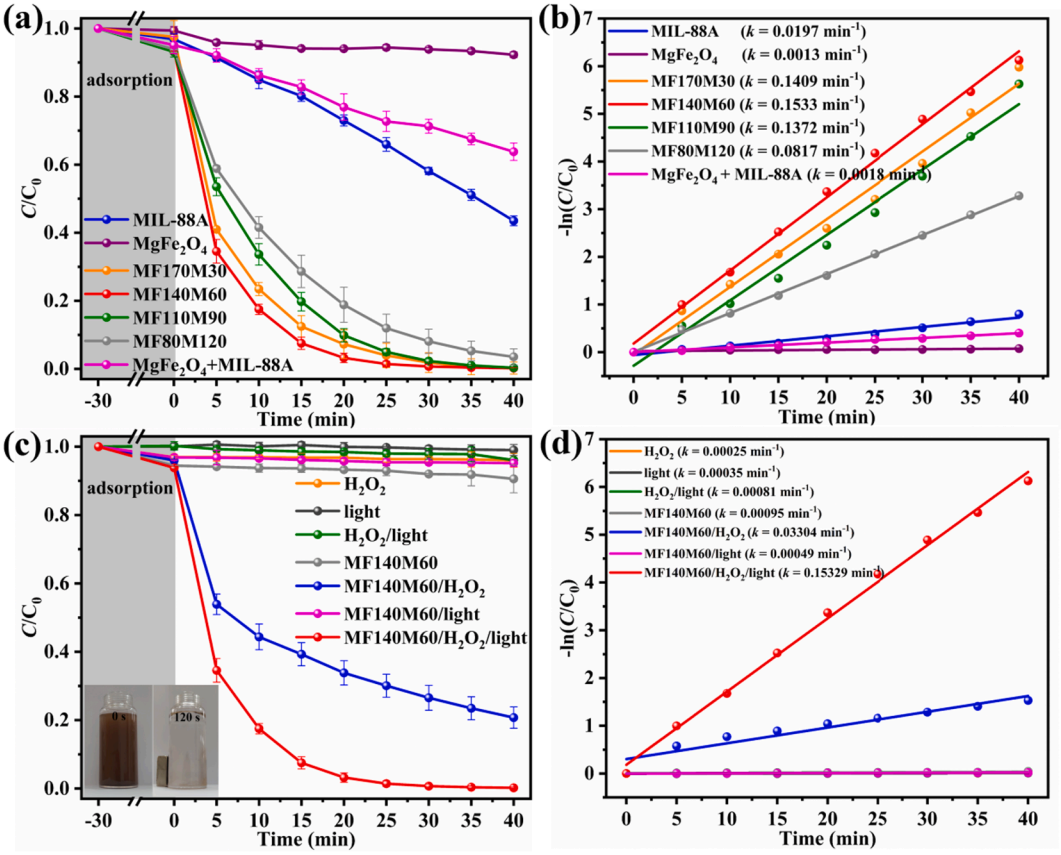

Fig. 5. (a) The SMX degradation efficiencies of different catalysts via photo-Fenton reactions under visible light. (b) The SMX degradation rates (*k* values) of different catalysts via photo-Fenton reactions under visible light. (c) The SMX degradation efficiencies in different systems. (d) The SMX degradation rates (*k* values) in different systems. Reaction conditions: catalysts dosage = 0.3 g/L, SMX concentration = 5.0 mg L^{-1}, volume = 50.0 mL, H_2O_2 = 2.94 mM, unadjusted pH = 5.8.

properties would make it possible to collect, recycle, and further reuse the MF140M60 catalyst.

3.3. The influences of key environmental factors on SMX degradation

3.3.1. Initial pH

The solution pH plays a crucial role in SMX removal in MF140M60/H_2O_2/light system as Fenton-like oxidation is dependent on acid-base conditions [50,51]. Fig. 6a displayed that 98.5% SMX decomposition efficiency could be achieved in 10.0 min at pH = 3, due to the acidic conditions could facilitate the formation of the •OH radicals for attacking the SMX [52–54] and produce more iron ions leaching to accelerate the reaction. At unadjusted pH (pH of 5.8), ca. 100% of SMX was degraded within 40 min. Though higher alkalinity would partly destroy the photo-Fenton system, 97.8% of SMX was degraded at pH = 9 within 40.0 min. Based on the above analysis, the MF140M60 materials can be applied over a broad pH range for the catalytic degradation of SMX, in which the weak acidic and neutral conditions were more beneficial for the catalytic reaction. In our work, unadjusted pH was selected to the corresponding experiments.

3.3.2. Catalyst dosage

Noticeably, with the same dosage of H_2O_2, the influence of MF140M60 dosages on SMX degradation results was shown in Fig. 6b. With MF140M60 dosage ranging from 0.2 g/L to 0.4 g/L, the SMX removal efficiencies were increased from 88.8% to 99.8% in 20 min,

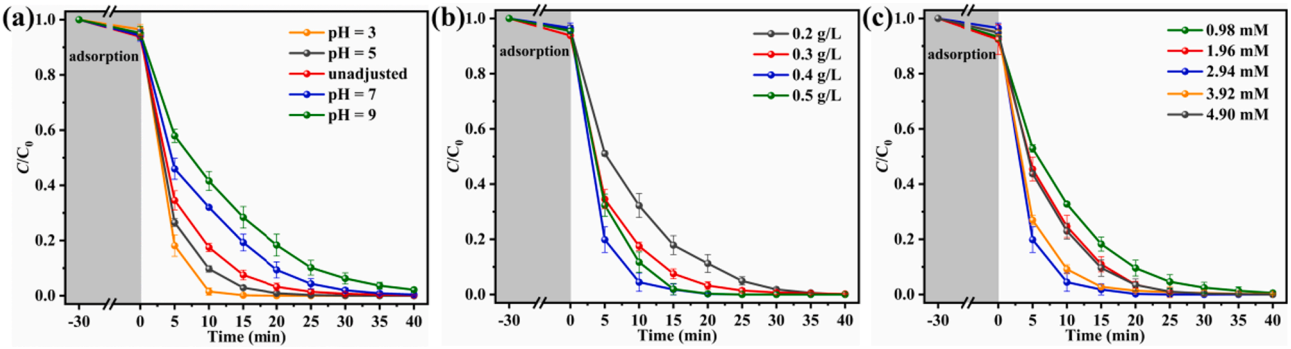

Fig. 6. Influences of (a) initial pH (b) catalyst dosage and (c) H_2O_2 concentration on the SMX degradation over MF140M60. Reaction conditions: catalysts dosage = 0.3 g/L for (a) and 0.4 g/L for (c), SMX concentration = 5.0 mg L^{-1}, volume = 50.0 mL, H_2O_2 = 2.94 mM (for a and b), unadjusted pH = 5.8 (for b and c).

confirming that the increasing catalyst dosage would provide more catalytic active sites for H_2O_2 activation to generate more hydroxyl radicals [54,55]. However, when the catalysts dosage further increased to 0.5 g/L, the SMX degradation efficiency decreased slightly, due to that the catalysts aggregation might reduce the available number of active sites and increase light scattering [56,57]. Given this, 0.4 g/L MF140M60 was used in the corresponding experiments.

3.3.3. The H_2O_2 concentration

Fig. 6c showed the effects of different dosages of H_2O_2 on SMX degradation results. With the increase of H_2O_2 concentration from 100 μL/L (0.98 mM) to 300 μL/L (2.94 mM), the SMX removal efficiency increased. The higher H_2O_2 concentration could capture the photo-induced electrons to inhibit the quick electron-hole recombination and yield more •OH radicals [58]. With H_2O_2 concentration increasing to 500 μL/L (4.90 mM), the degradation efficiency of SMX decreased slightly. The radicals at a higher H_2O_2 concentration might undergo a self-quenching. The degradation efficiency was not further improved and the degradation rate became slower, possibly resulting from the •OH consumption by surplus H_2O_2 to form less reactive species (Eq. (1)) [54]. Therefore, 2.94 mM H_2O_2 were used in the corresponding experiments.

$$H_2O_2 + \bullet OH \rightarrow HOO\bullet + H_2O_2 \rightarrow H_2O + O_2 \quad (1)$$

3.3.4. The co-existing ions

The co-existing ions might impact the SMX degradation during the photo-Fenton process, which was explored by the Box-Behnken experimental design methodology [59]. The four independent variables such as (A) Cl^-, (B) NO_3^-, (c) HCO_3^- and (D) SO_4^{2-} were selected as experimental variables to clarify the influences on the SMX degradation efficiencies over MF140M60 under LED visible light (Fig. 7). The concentration of the four above-stated factors based on the wastewater samples from a wastewater treatment plant effluent: [Cl^-] = 71.0 mg/L, [NO_3^-] = 7.1 mg/L, [HCO_3^-] = 22.0 mg/L, [SO_4^{2-}] = 32.0 mg/L [60,61]. As listed in Table. S1 and S2, 29 groups of experiments were taken out, in which the response (degradation efficiency %) and independent variables matched well with the quadratic polynomial model as listed in Eq. (2).

$$\begin{aligned}\text{Efficiency}\,\% = {} & 53.94 - 3.23A + 1.18B - 35.26C - 2.70D + 2.18AB \\ & - 4.85AC - 2.38AD + 12.10BC + 0.45BD - 6.96CD \\ & + 11.18A^2 + 3.04B^2 + 1.19C^2 + 3.84D^2 \end{aligned} \quad (2)$$

The R^2 reflected the variability of the dependent variable, which can be explained by its relationship with the independent process variables. Based on the ANOVA results of photo-Fenton efficiencies, the R^2 and adjusted R^2 were calculated as 0.9799 and 0.9598, respectively, demonstrating close agreement of the experimental and theoretical values of the response (Table. S3). As well, the influences of four variables on SMX degradation according to the F values of variables followed the order of C (602.48) > A (5.05) > D (3.54) > B (0.67), implying that the HCO_3^- was the most important variable, while other three ions exerted insignificant influence. It was deemed that the HCO_3^- anions could act as buffer mediate [62] and as •OH scavenger [63]. Moreover, some magnetic materials applied in photo-Fenton wastewater treatment are listed (Table. S4), in which the as-prepared MF140M60 as catalyst displayed good performance.

3.4. The possible degradation mechanisms

In general, photoluminescence (PL) analysis was introduced to evaluate the recombination of photoinduced electrons and holes, in which a low PL intensity implied a slow recombination rate of charge carriers [64,65]. As shown in Fig. 8a, the PL emission of pure $MgFe_2O_4$ and MIL-88A was strong, while the emission peaks of MF140M60 decreased, implying that the formation of the $MgFe_2O_4$/MIL-88A heterostructure would boost the separation of the photoinduced carriers for the improved catalytic activity.

The electrochemical impedance spectroscope (EIS) measurements could be performed to examine the interfacial charge transfer of various

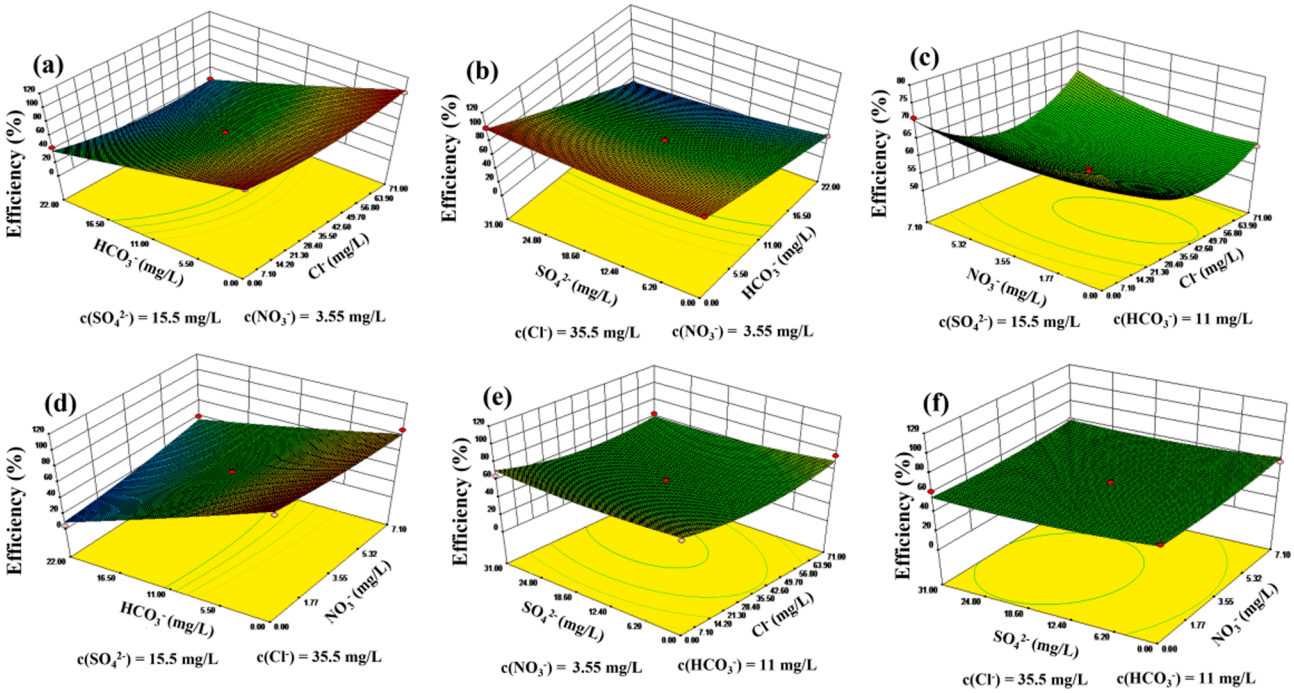

Fig. 7. Response surface graphs of different co-existing ions like Cl^-, NO_3^-, SO_4^{2-} and HCO_3^- on SMX degradation activities of MF140M60. Reaction conditions: catalysts dosage = 0.4 g/L, SMX concentration = 5.0 mg L^{-1}, volume = 50.0 mL, H_2O_2 = 2.94 mM, unadjusted pH = 5.8.

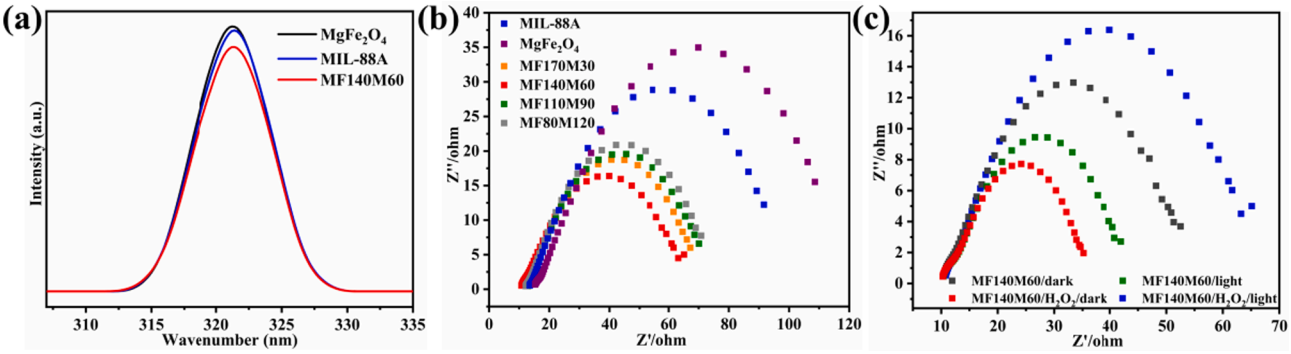

Fig. 8. (a) The PL spectra of different catalysts. The EIS analysis of (b) different catalysts and (c) MF140M60 in different conditions.

photocatalysts. The MF140M60 displayed smaller charge transfer resistance [62], as its Nyquist arc radius was smaller than those of $MgFe_2O_4$, MIL-88A and other composites (Fig. 8b). The experimental result proved the ratio of $MgFe_2O_4$ and MIL-88A could change the charge carrier separation and catalytic activity, which agreed with the results of SMX degradation degree. Moreover, the synergistic effects of MF140M60, visible light and H_2O_2 resulted into decreasing resistance for the enhanced electron transfer (Fig. 8c). The photo current response of MF140M60/H_2O_2 increased significantly than that of $MgFe_2O_4$/H_2O_2 and MIL-88A/H_2O_2 (Fig. S4), implying the combination of $MgFe_2O_4$ and MIL-88A could quicker the transfer rate of holes and electrons [63].

To further understand the active species that participated in the SMX degradation process, different radical scavengers were introduced to detect the existence of active species (Fig. 9a). The *tert*-butanol (TBA), N_2, furfuryl alcohol (FFA) and D_2O were selected to trap •OH, $\bullet O_2^-$ and $^1O_2$, respectively [66–68]. As illustrated in Fig. 9a, the addition of 50 mM TBA resulted in a dramatically decreased SMX removal to 11.5%, affirming that •OH would be primary active specie in the system. In the presence 50 mM furyl alcohol (FFA), the SMX degradation efficiency was decreased to 37.5%. The SMX degradation efficiency in D_2O solution was superior to that in aqueous solution, due to that lifetime of the $^1O_2$ in D_2O is longer than that in H_2O [69]. It was implied that the formed $^1O_2$ made contribution to the SMX degradation. Besides, the presence of 0.1 mM β-Carotene or 0.2 mM L-histidine also could severely hinder the degradation efficiency (Fig. S5), further implying the non-radical $^1O_2$ played a significant role in the system [70]. However, little degradation efficiency decrease was observed in the presence of N_2 and 1 mM oxalic acid (OA), respectively, indicating that $\bullet O_2^-$ and h^+ acted as minor role in this photo-Fenton system.

The presence of •OH radicals also can be affirmed by a fluorescence method adopting terephthalic acid as probe [71]. The experiment processes were like the photo-Fenton experiment except that a solution of 2 mM NaOH and 0.5 mM terephthalic acid was used instead of the original SMX solution. As shown in Fig. 9b and c, the fluorescence intensity of

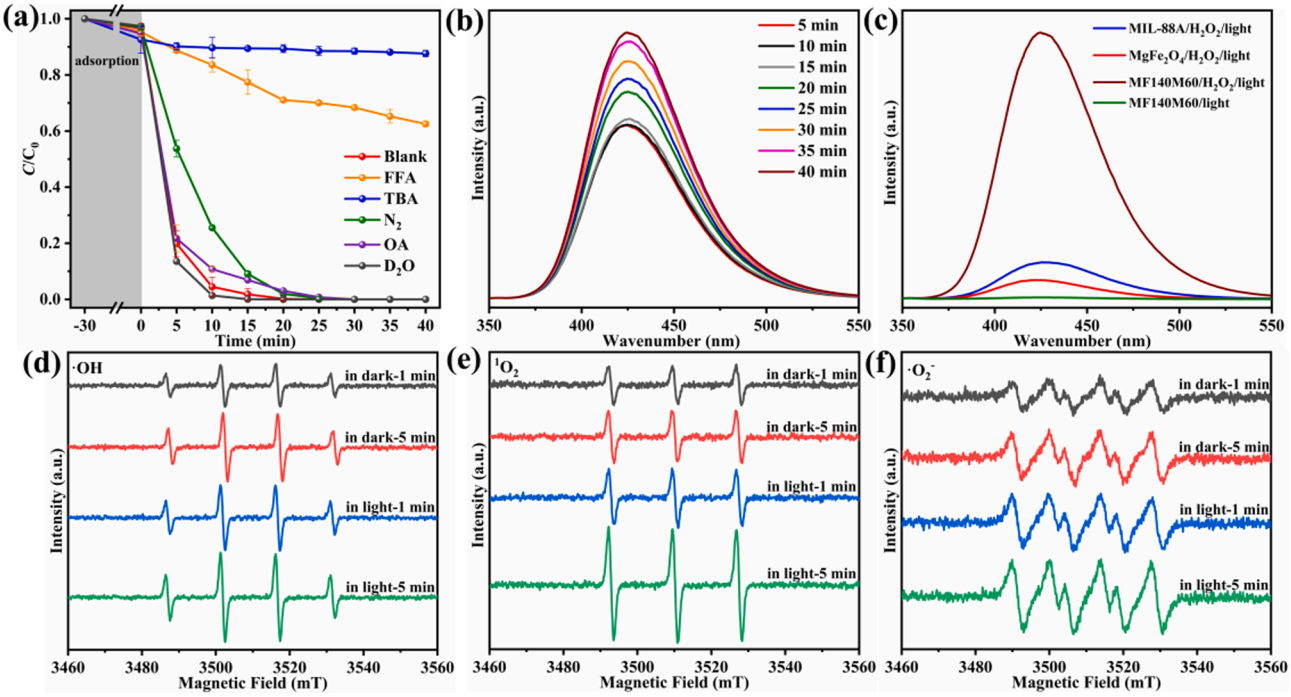

Fig. 9. (a) Effects of different scavengers on SMX degradation in the presence of MF140M60. (b) Different times and (c) systems of fluorescence emission spectra of •OH radicals generated at 315 nm. The ESR spectra of (d) DMPO-•OH (e) TEMP-$^1O_2$ and (f) DMPO-$\bullet O_2^-$ over MF140M60 with the presence of H_2O_2. Reaction conditions of Fig. 9a: catalysts dosage = 0.4 g/L, SMX concentration = 5.0 mg L^{-1}, volume = 50.0 mL, H_2O_2 = 2.94 mM, unadjusted pH = 5.8.

formed 2-hydroxy terephthalic acid MF140M60/H_2O_2/light system increased gradually, implying increasing •OH radicals can be continuously generated with the reaction time and MF140M60/H_2O_2 could produce more •OH radicals.

Compared to $MgFe_2O_4$ and MIL-88A, a relatively higher H_2O_2 consumption efficiency was achieved over the MF140M60 (Fig. S6). The as-formed heterojunction could reduce the recombination of charge carriers, in which the photo-induced electrons are more easily trapped by H_2O_2 to boost the consumption of H_2O_2 [72]. Furthermore, the electron spin resonance (ESR) tests with 5, 5-dimethyl-1-pyrroline (DMPO) and 2, 6, 6-tetramethyl-4-piperidone (TEMP) as a radical spin trapping agent were performed to identify the active species. As shown in Fig. 9d, e and f, it can be observed that the characteristic ESR signals of •OH, $^1O_2$ and $•O_2^-$ at 5 min were stronger than those at 1 min under both dark and light systems, displaying that •OH, $^1O_2$ and $•O_2^-$ could produce during the dark Fenton and photo-Fenton systems. As expected, the light irradiation could promote the transfer of photogenerated electrons, thus producing more •OH, $^1O_2$ and $•O_2^-$ signals.

The flat band potentials (E_{FB}) of individual MIL-88A and $MgFe_2O_4$ were determined by using Mott-Schottky plots. As shown in Fig. 10a and b, the positive correlations between the potentials and the C^{-2} of both MIL-88A and $MgFe_2O_4$ at different frequencies of 500, 1000 and 1500 Hz indicated that both of them are typical n-type catalysts [73]. Besides, the flat-band potential for MIL-88A and $MgFe_2O_4$ were −0.55 eV and −0.72 eV versus Ag/AgCl, which are calculated as −0.35 eV and −0.52 eV versus the normal hydrogen electrode (NHE) [74]. For n-type semiconductors, its E_{FB} potential was more positive ca. 0.1 eV than the conduction band (E_{CB}) potential [75]. Therefore, the E_{LUMO} of MIL-88A and E_{CB} of $MgFe_2O_4$ were −0.45 eV and −0.62 eV, which were consist with the previous reports [26,76]. In addition, the E_{VB} potential of the semiconductor can be calculated based on the formula of $E_g = E_{VB} - E_{CB}$. Thus, the E_{VB} potential of MIL-88A and $MgFe_2O_4$ was calculated as 2.30 eV and 1.10 eV *vs.* NHE, respectively.

The possible mechanism of SMX degradation by MF140M60 was proposed. As shown in Fig. 10c, upon the illumination of visible light, both MIL-88A and $MgFe_2O_4$ were excited to produce photogenerated electrons and holes (Eqs. 3 and 4). Due to the heterostructure between the MIL-88A and $MgFe_2O_4$, the electrons on the CB of $MgFe_2O_4$ could transfer to the LUMO of MIL-88A. The LUMO potential of the MIL-88A was determined as −0.45 eV, indicating that the electrons could react with the dissolved oxygen (DO) to yield $•O_2^-$ ($O_2/•O_2^- = -0.33$ eV) (Eq. 5). Furthermore, h^+ could oxidize SMX directly. H_2O_2 could capture e^- to produce •OH for SMX degradation (Eq. 6). The •OH could further react with H_2O_2 to form $^1O_2$ [77]. Finally, the transformation between Fe(III) and Fe(II) could also activate H_2O_2 to produce increasing •OH radicals (Eqs. 7 and 8), in which the existence of Fe(II) could be confirmed by XPS of used MF140M60 (Fig. S7). The h^+, $•O_2^-$, •OH and $^1O_2$ could attack pollution directly (Eq. 9).

$$MIL\text{-}88A + h\nu \rightarrow h^+ + e^- \quad (3)$$

$$MgFe_2O_4 + h\nu \rightarrow h^+ + e^- \quad (4)$$

$$O_2 + e^- \rightarrow •O_2^- \quad (5)$$

$$H_2O_2 + e^- \rightarrow •OH \quad (6)$$

$$Fe(III) + H_2O_2 \rightarrow Fe(II) + •HOO/•O_2^- + H^+ \quad (7)$$

$$Fe(II) + H_2O_2 \rightarrow Fe(III) + •OH + OH^- \quad (8)$$

$$h^+, •O_2^-, •OH, {}^1O_2 \text{ attack pollutant} \rightarrow \text{degradation intermediate} \quad (9)$$

3.5. Reusability of catalyst

Considering the capacity for the actual application of the catalyst, it was essential to evaluate its recycling performance. Using the recovered MF140M60 as the catalyst, 5 consecutive cycles of activating H_2O_2 to degrade SMX were conducted. Fig. 11a depicted the experimental outcomes of the as-prepared catalyst MF140M60 under five times recycled degradation process. It was worth noting that the reaction rate of SMX dropped slightly, but the catalyst still showed high activity in SMX removal, implying its high efficiency and good stability in H_2O_2 oxidation. The ICP-OES was used to determine the leaching Fe in different cycles of MF140M60 during the catalytic reaction (Fig. 11b). In our work, the leached Fe ion concentrations ranged from 0.58 mg/L to 0.80 mg/L of each cycle, which were lower than the integrated discharge standard of water pollutants (2.0 mg/L) set by the Beijing local standard (DB11/307–2013). The stable structure and morphology of the catalyst after five-cycle experiments were affirmed by SEM and PXRD (Fig. 11c and d).

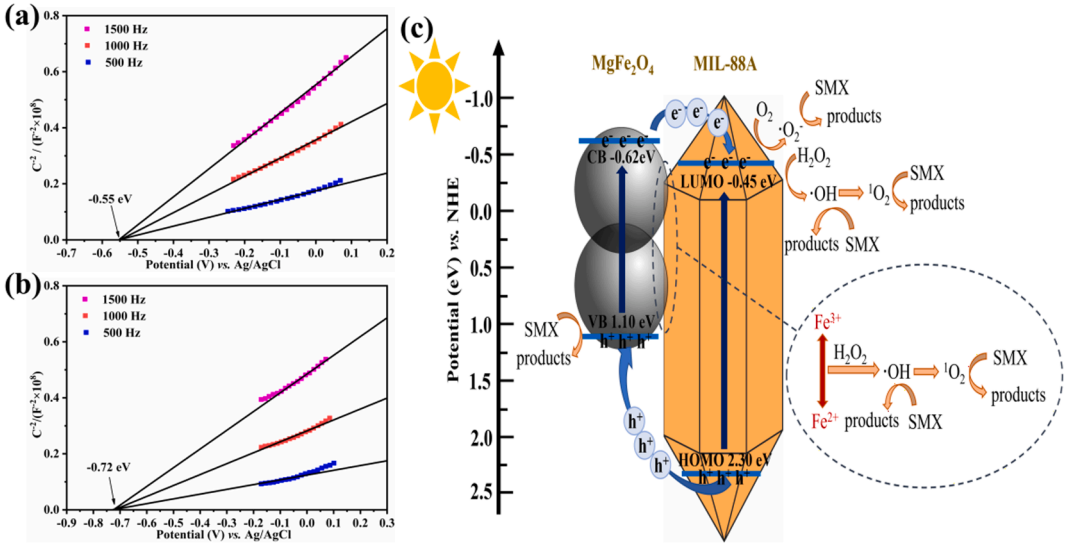

Fig. 10. The Mott-Schottky plots of (a) MIL-88A and (b) $MgFe_2O_4$ at different frequencies. (c) Mechanistic scheme of photo-Fenton reaction over $MgFe_2O_4$/MIL-88A.

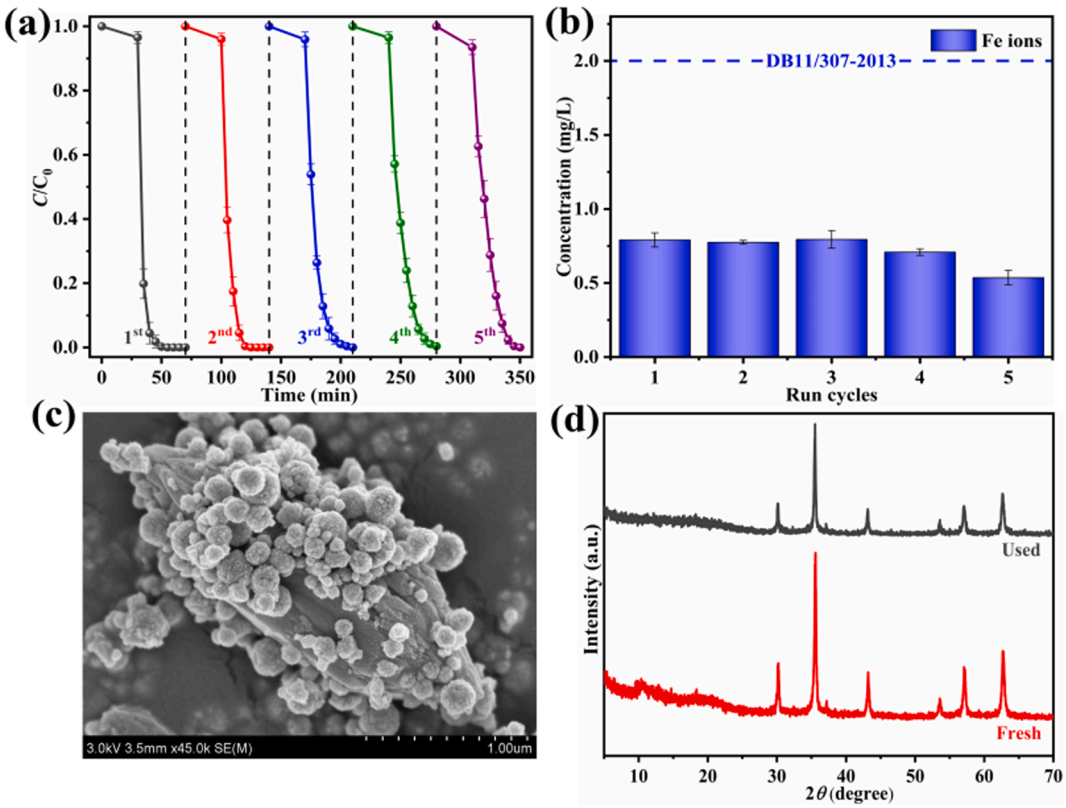

Fig. 11. (a) Photo-Fenton SMX degradation efficiencies over MF140M60 in five consecutive runs under LED visible light. (b) Ion leaching concentrations of MF140M60 determined by ICP-OES, (c) SEM and (d) PXRD of MF140M60 after photo-Fenton degradation toward SMX.

4. Conclusion

Series of $MgFe_2O_4$/MIL-88A composites were synthesized by simple ball-milling method and their photo-Fenton SMX performances were tested. The performance of the composites was significantly improved compared to pure $MgFe_2O_4$ and MIL-88A, and the optimum ratio of MF140M60 degraded 99.8% of 5 ppm SMX within 20 min. The effects of initial pH, H_2O_2 dosing and coexisting inorganic anions on the degradation of SMX by MF140M60 were investigated. 100% degradation efficiencies were maintained for 5 rounds of catalysis experiments, which demonstrated the stability of the as-prepared MF140M60. Finally, the reaction mechanism of photo-Fenton degradation of SMX over MF140M60 was clarified by electrochemical characterization, active material capture, ESR analysis. The MF140M60 catalyst might be potentially used to remove the organic pollutants in the real wastewater treatment.

CRediT authorship contribution statement

Ke-Xin Shi: Data curation, Investigation, Visualization, Software, Writing – original draft. **Fuguo Qiu:** Resources, Validation. **Peng Wang:** Resources. **Haiyan Li:** Resources. **Chong-Chen Wang:** Conceptualization, Funding acquisition, Supervision, Project administration, Writing – review & editing.

Declaration of Competing Interest

The authors declare that they have no known competing financial interests or personal relationships that could have appeared to influence the work reported in this paper.

Data availability

Data will be made available on request.

Acknowledgments

This work was supported by National Natural Science Foundation of China [22176012, 51878023], Beijing Natural Science Foundation [8202016], Beijing Talent Project [2020A27], Science and Technology General Project of Beijing Municipal Education Commission [KM202110016010], The Fundamental Research Funds for Beijing University of Civil Engineering and Architecture [X20147, X20141, X20135, X20146] and BUCEA Post Graduate Innovation Project [PG2022057].

Appendix A. Supplementary material

Supplementary data to this article can be found online at https://doi.org/10.1016/j.seppur.2022.121965.

References

[1] L. Shi, Z. Hu, W.S. Simplicio, S. Qiu, L. Xiao, B. Harhen, X. Zhan, Antibiotics in nutrient recovery from pig manure via electrodialysis reversal: sorption and migration associated with membrane fouling, J. Membr. Sci. 597 (2020) 117633, https://doi.org/10.1016/j.memsci.2019.117633.

[2] X.-J. Yu, Y.-W. Miao, H.-B. Li, Q. Su, K.-L. Liu, L.-Y. Fu, Y.-K. Hou, X.-L. Shi, Y. Li, J.-J. Mu, W.-S. Chen, W. Cui, G.-Q. Zhu, P.J. Ebenezer, J. Francis, Y.-M. Kang, Blockade of endogenous angiotensin-(1–7) in hypothalamic paraventricular nucleus attenuates high salt-induced sympathoexcitation and hypertension, Neurosci. Bull. 35 (1) (2019) 47–56, https://doi.org/10.1007/s12264-018-0297-4.

[3] E. Kassotaki, G. Buttiglieri, L. Ferrando-Climent, I. Rodriguez-Roda, M. Pijuan, Enhanced sulfamethoxazole degradation through ammonia oxidizing bacteria co-metabolism and fate of transformation products, Water Res. 94 (2016) 111–119, https://doi.org/10.1016/j.watres.2016.02.022.

[4] J. Wang, R. Zhuan, L. Chu, The occurrence, distribution and degradation of antibiotics by ionizing radiation: an overview, Sci. Total Environ. 646 (2019) 1385–1397, https://doi.org/10.1016/j.scitotenv.2018.07.415.

[5] I. Ahmed, B.N. Bhadra, H.J. Lee, S.H. Jhung, Metal-organic framework-derived carbons: preparation from ZIF-8 and application in the adsorptive removal of sulfamethoxazole from water, Catal. Today 301 (2018) 90–97, https://doi.org/10.1016/j.cattod.2017.02.011.

[6] F. Pomati, S. Castiglioni, E. Zuccato, R. Fanelli, D. Vigetti, C. Rossetti, D. Calamari, Effects of a complex mixture of therapeutic drugs at environmental levels on human embryonic cells, Environ. Sci. Technol. 40 (2006) 2442–2447, https://doi.org/10.1021/es051715a.

[7] M. Qi, B. Liang, L. Zhang, X. Ma, L. Yan, W. Dong, D. Kong, L. Zhang, H. Zhu, S.-H. Gao, J. Jiang, S.-J. Liu, P.-X. Corvini, A. Wang, Microbial interactions drive the complete catabolism of the antibiotic sulfamethoxazole in activated sludge microbiomes, Environ. Sci. Technol. 55 (5) (2021) 3270–3282, https://doi.org/10.1021/acs.est.0c06687.

[8] F. Reguyal, A.K. Sarmah, Adsorption of sulfamethoxazole by magnetic biochar: effects of pH, ionic strength, natural organic matter and 17α-ethinylestradiol, Sci. Total Environ. 628 (2018) 722–730, https://doi.org/10.1016/j.scitotenv.2018.01.323.

[9] F. Qian, H. Yin, F. Liu, J. Sheng, S. Gao, Y. Shen, The in situ catalytic oxidation of sulfamethoxazole via peroxydisufate activation operated in a NG/rGO/CNTs composite membrane filtration, Environ. Sci. Pollut. R. 28 (2021) 26828–26839, https://doi.org/10.1007/s11356-021-12545-1.

[10] Y.-Q. Gao, N.-Y. Gao, Y. Deng, D.-Q. Yin, Y.-S. Zhang, W.-L. Rong, S.-D. Zhou, Heat-activated persulfate oxidation of sulfamethoxazole in water, Desalin. Water Treat. 56 (2015) 2225–2233, https://doi.org/10.1080/19443994.2014.960471.

[11] Q. Zhao, C.-C. Wang, P. Wang, Effective norfloxacin elimination via photo-Fenton process over the MIL-101(Fe)-NH_2 immobilized on α-Al_2O_3 sheet, Chin. Chem. Lett. 33 (2022) 4828–4833, https://doi.org/10.1016/j.cclet.2022.01.033.

[12] J.-S. Wang, X.-H. Yi, X. Xu, H. Ji, A.M. Alanazi, C.-C. Wang, C. Zhao, Y.V. Kaneti, P. Wang, W. Liu, Y. Yamauchi, Eliminating tetracycline antibiotics matrix via photoactivated sulfate radical-based advanced oxidation process over the immobilized MIL-88A: Batch and continuous experiments, Chem. Eng. J. 431 (2022) 133213, https://doi.org/10.1016/j.cej.2021.133213.

[13] A. Du, H. Fu, P. Wang, C. Zhao, C.C. Wang, Enhanced catalytic peroxymonosulfate activation for sulfonamide antibiotics degradation over the supported CoSx-CuSx derived from ZIF-L(Co) immobilized on copper foam, J. Hazard. Mater. 426 (2022) 128134, https://doi.org/10.1016/j.jhazmat.2021.128134.

[14] H.-Y. Chu, T.-Y. Wang, C.-C. Wang, Advanced Oxidation Processes (AOPs) for bacteria removal over MOFs-based materials, Prog. Chem. (in press). doi:10.7536/220501.

[15] X.-H. Yi, C.-C. Wang, Elimination of emerging organic contaminants in wastewater by advanced oxidation process over iron-based MOFs and their composites, Prog. Chem. 33 (2021) 471–489, https://doi.org/10.7536/PC200562.

[16] J. Fang, X. Huang, Q. Zhang, J. Chen, X. Wang, Study on the surface speciation of Fe-pillared montmorillonite and mechanism of its photocatalytic effect on degradation of ionic dye rhodamine-B, Appl. Surf. Sci. 360 (2016) 994–998, https://doi.org/10.1016/j.apsusc.2015.11.102.

[17] Y. Fu, K. Zhang, Y. Zhang, Y. Cong, Q. Wang, Fabrication of visible-light-active MR/NH_2-MIL-125(Ti) homojunction with boosted photocatalytic performance, Chem. Eng. J. 412 (2021) 128722, https://doi.org/10.1016/j.cej.2021.128722.

[18] Y.-H. Li, C.-C. Wang, X.u. Zeng, X.-Z. Sun, C. Zhao, H. Fu, P. Wang, Seignette salt induced defects in Zr-MOFs for boosted Pb(II) adsorption: universal strategy and mechanism insight, Chem. Eng. J. 442 (2022) 136276, https://doi.org/10.1016/j.cej.2022.136276.

[19] C.-Y. Wang, L. Ma, C.-C. Wang, P. Wang, L. Gutierrez, W. Zheng, Light-response adsorption and desorption behaviors of metal–organic frameworks, Environ. Funct. Mater. 1 (2022) 49–66, https://doi.org/10.1016/j.efmat.2022.05.002.

[20] J. Hang, X.H. Yi, C.C. Wang, H. Fu, P. Wang, Y. Zhao, Heterogeneous photo-Fenton degradation toward sulfonamide matrix over magnetic Fe_3S_4 derived from MIL-100 (Fe), J. Hazard. Mater. 424 (2022) 127415, https://doi.org/10.1016/j.jhazmat.2021.127415.

[21] N. Liu, W. Huang, X. Zhang, L. Tang, L. Wang, Y. Wang, M. Wu, Ultrathin graphene oxide encapsulated in uniform MIL-88A(Fe) for enhanced visible light-driven photodegradation of RhB, Appl. Catal. B: Environ. 221 (2018) 119–128, https://doi.org/10.1016/j.apcatb.2017.09.020.

[22] X. He, H. Fang, D.J. Gosztola, Z. Jiang, P. Jena, W.-N. Wang, Mechanistic insight into photocatalytic pathways of MIL-100 (Fe)/TiO_2 composites, ACS Appl. Mater. Int. 11 (2019) 12516–12524, https://doi.org/10.1021/acsami.9b00223.

[23] D. Wang, M. Wang, Z. Li, Fe-based metal-organic frameworks for highly selective photocatalytic benzene hydroxylation to phenol, ACS Catal. 5 (2015) 6852–6857, https://doi.org/10.1021/acscatal.5b01949.

[24] H. Fu, X.-X. Song, L. Wu, C. Zhao, P. Wang, C.-C. Wang, Room-temperature preparation of MIL-88A as a heterogeneous photo-Fenton catalyst for degradation of rhodamine B and bisphenol a under visible light, Mater. Res. Bull. 125 (2020) 110806, https://doi.org/10.1016/j.materresbull.2020.110806.

[25] J.-F. Wang, Y. Liu, P. Shao, Z.-Y. Zhu, H.-D. Ji, Z.-X. Du, C.-C. Wang, W. Liu, L.-J. Gao, Efficient ofloxacin degradation via photo-Fenton process over eco-friendly MIL-88A(Fe): Performance, degradation pathways, intermediate library establishment and toxicity evaluation, Environ. Res. 210 (2022) 112937, https://doi.org/10.1016/j.envres.2022.112937.

[26] D.D. Chen, X.H. Yi, L. Ling, C.C. Wang, P. Wang, Photocatalytic Cr(VI) sequestration and photo-Fenton bisphenol A decomposition over white light responsive PANI/MIL-88A(Fe), Appl. Organomet. Chem. 34 (2020) e5795, https://doi.org/10.1002/aoc.5795.

[27] S. Shi, X. Han, J. Liu, X. Lan, J. Feng, Y. Li, W. Zhang, J. Wang, Photothermal-boosted effect of binary CuFe bimetallic magnetic MOF heterojunction for high-performance photo-Fenton degradation of organic pollutants, Sci. Total Environ. 795 (2021) 148883, https://doi.org/10.1016/j.scitotenv.2021.148883.

[28] Z. Xiong, H. Zheng, Y. Hu, X. Hu, W. Ding, J. Ma, Y. Li, Selective adsorption of Congo red and Cu(II) from complex wastewater by core-shell structured magnetic carbon@zeolitic imidazolate frameworks-8 nanocomposites, Sep. Purif. Technol. 277 (2021) 119053, https://doi.org/10.1016/j.seppur.2021.119053.

[29] L. Dong, Y. Li, D. Chen, X. Chen, D. Zhang, Facilitated activation of peroxymonosulfate by loading ZIF-8 on Fe_3O_4-MnO_2 for deep mineralization of bisphenol A, ACS ES&T Water 1 (2020) 417–429, https://doi.org/10.1021/acsestwater.0c00169.

[30] X. Wu, D. Sun, H. Ma, C. Ma, X. Zhang, J. Hao, Activation of peroxymonosulfate by magnetic $CuFe_2O_4$@ZIF-67 composite catalyst for the study on the degradation of methylene blue, Colloids Surf. A 637 (2022) 128278, https://doi.org/10.1016/j.colsurfa.2022.128278.

[31] S. Bargozideh, M. Tasviri, S. Shekarabi, H. Daneshgar, Magnetic $BiFeO_3$ decorated UiO-66 as a p–n heterojunction photocatalyst for simultaneous degradation of a binary mixture of anionic and cationic dyes, New J. Chem. 44 (2020) 13083–13092, https://doi.org/10.1039/d0nj02594a.

[32] J. Gu, Q. Li, X. Long, X. Zhou, N. Liu, Z. Li, Fabrication of magnetic dual Z-scheme heterojunction materials for efficient photocatalytic performance: the study of ternary novel MIL-88A (Fe)/BiOBr/$SrFe_{12}O_{19}$ nanocomposite, Sep. Purif. Technol. 289 (2022) 120778, https://doi.org/10.1016/j.seppur.2022.120778.

[33] Z. Liao, M. Ma, Y. Bi, Z. Tong, K.L. Chung, Z. Li, Y. Ma, B. Gao, Z. Cao, R. Sun, X. Zhong, MoS_2 decorated on one-dimensional $MgFe_2O_4$/MgO/C composites for high-performance microwave absorption, J. Colloid Interface Sci. 606 (2022) 709–718, https://doi.org/10.1016/j.jcis.2021.08.056.

[34] B. Yao, Z. Luo, S. Du, J. Yang, D. Zhi, Y. Zhou, Sustainable biochar/$MgFe_2O_4$ adsorbent for levofloxacin removal: adsorption performances and mechanisms, Bioresour. Technol. 340 (2021) 125698, https://doi.org/10.1016/j.biortech.2021.125698.

[35] L. Zhao, X. Li, Q. Zhao, Z. Qu, D. Yuan, S. Liu, X. Hu, G. Chen, Synthesis, characterization and adsorptive performance of $MgFe_2O_4$ nanospheres for SO_2 removal, J. Hazard. Mater. 184 (2010) 704–709, https://doi.org/10.1016/j.jhazmat.2010.08.096.

[36] X.-H. Yi, H. Ji, C.-C. Wang, Y. Li, Y.-H. Li, C. Zhao, A.o. Wang, H. Fu, P. Wang, X. u. Zhao, W. Liu, Photocatalysis-activated SR-AOP over PDINH/MIL-88A(Fe) composites for boosted chloroquine phosphate degradation: performance, mechanism, pathway and DFT calculations, Appl. Catal. B: Environ. 293 (2021) 120229, https://doi.org/10.1016/j.apcatb.2021.120229.

[37] R. Yuan, J. Qiu, C. Yue, C. Shen, D. Li, C. Zhu, F. Liu, A. Li, Self-assembled hierarchical and bifunctional MIL-88A(Fe)@$ZnIn_2S_4$ heterostructure as a reusable sunlight-driven photocatalyst for highly efficient water purification, Chem. Eng. J. 401 (2020) 126020, https://doi.org/10.1016/j.cej.2020.126020.

[38] K.-Y. Andrew Lin, H.-A. Chang, C.-J. Hsu, Iron-based metal organic framework, MIL-88A, as a heterogeneous persulfate catalyst for decolorization of Rhodamine B in water, RSC Adv. 5 (2015) 32520–32530, https://doi.org/10.1039/c5ra01447f.

[39] Y. Zhang, J. Zhou, X. Chen, L. Wang, W. Cai, Coupling of heterogeneous advanced oxidation processes and photocatalysis in efficient degradation of tetracycline hydrochloride by Fe-based MOFs: synergistic effect and degradation pathway, Chem. Eng. J. 369 (2019) 745–757, https://doi.org/10.1016/j.cej.2019.03.108.

[40] D. Kang, X. Yu, M. Ge, W. Song, One-step fabrication and characterization of hierarchical $MgFe_2O_4$ microspheres and their application for lead removal, Micropor. Mesopor. Mat. 207 (2015) 170–178, https://doi.org/10.1016/j.micromeso.2015.01.023.

[41] Y. Liang, R. Shang, J. Lu, L. Liu, J. Hu, W. Cui, Ag_3PO_4@UMOFNs core-shell structure: two-dimensional MOFs promoted photoinduced charge separation and photocatalysis, ACS Appl. Mater. Int. 10 (2018) 8758–8769, https://doi.org/10.1021/acsami.8b00198.

[42] G. Ren, K. Zhao, L. Zhao, A Fenton-like method using ZnO doped MIL-88A for degradation of methylene blue dyes, RSC Adv. 10 (2020) 39973–39980, https://doi.org/10.1039/D0RA08076D.

[43] K.D. McDonald, B.M. Bartlett, Microwave synthesis of spinel $MgFe_2O_4$ nanoparticles and the effect of annealing on photocatalysis, Inorg. Chem. 60 (2021) 8704–8709, https://doi.org/10.1021/acs.inorgchem.1c00663.

[44] V.P. Viswanathan, K. Divya, D.P. Dubal, N.N. Adarsh, S. Mathew, Ag/AgCl@ MIL-88A (Fe) heterojunction ternary composites: towards the photocatalytic degradation of organic pollutants, Dalton Trans. 50 (2021) 2891–2902, https://doi.org/10.1039/D0DT03147J.

[45] J. Jia, X. Du, Q. Zhang, E. Liu, J. Fan, Z-scheme $MgFe_2O_4$/Bi_2MoO_6 heterojunction photocatalyst with enhanced visible light photocatalytic activity for malachite green removal, Appl. Surf. Sci. 492 (2019) 527–539, https://doi.org/10.1016/j.apsusc.2019.06.258.

[46] X.-H. Yi, S.-Q. Ma, X.-D. Du, C. Zhao, H. Fu, P. Wang, C.-C. Wang, The facile fabrication of 2D/3D Z-scheme g-C_3N_4/UiO-66 heterojunction with enhanced photocatalytic Cr(VI) reduction performance under white light, Chem. Eng. J. 375 (2019) 121944, https://doi.org/10.1016/j.cej.2019.121944.

[47] Z. Jiang, K. Chen, Y. Zhang, Y. Wang, F. Wang, G. Zhang, D.D. Dionysiou, Magnetically recoverable $MgFe_2O_4$/conjugated polyvinyl chloride derivative nanocomposite with higher visible-light photocatalytic activity for treating Cr(VI)-polluted water, Sep. Purif. Technol. 236 (2020) 116272, https://doi.org/10.1016/j.seppur.2019.116272.

[48] X. Jiang, S. Su, J. Rao, S. Li, T. Lei, H. Bai, S. Wang, X. Yang, Magnetic metal-organic framework (Fe_3O_4@ZIF-8) core-shell composite for the efficient removal of

Pb(II) and Cu(II) from water, J. Environ. Chem. Eng. 9 (5) (2021) 105959, https://doi.org/10.1016/j.jece.2021.105959.
[49] K. Zhang, D. Sun, C. Ma, G. Wang, X. Dong, X. Zhang, Activation of peroxymonosulfate by $CoFe_2O_4$ loaded on metal-organic framework for the degradation of organic dye, Chemosphere 241 (2020) 125021, https://doi.org/10.1016/j.chemosphere.2019.125021.
[50] J.J. Pignatello, E. Oliveros, A. MacKay, Advanced oxidation processes for organic contaminant destruction based on the fenton reaction and related chemistry, Crit. Rev. Env. Sci. Tec. 36 (2006) 1–84, https://doi.org/10.1080/10643380500326564.
[51] M. Wang, G. Fang, P. Liu, D. Zhou, C. Ma, D. Zhang, J. Zhan, Fe_3O_4@β-CD nanocomposite as heterogeneous Fenton-like catalyst for enhanced degradation of 4-chlorophenol (4-CP), Appl. Catal. B: Environ. 188 (2016) 113–122, https://doi.org/10.1016/j.apcatb.2016.01.071.
[52] N.K. Daud, B.H. Hameed, Decolorization of Acid Red 1 by Fenton-like process using rice husk ash-based catalyst, J. Hazard. Mater. 176 (2010) 938–944, https://doi.org/10.1016/j.jhazmat.2009.11.130.
[53] M. Kallel, C. Belaid, T. Mechichi, M. Ksibi, B. Elleuch, Removal of organic load and phenolic compounds from olive mill wastewater by Fenton oxidation with zero-valent iron, Chem. Eng. J. 150 (2009) 391–395, https://doi.org/10.1016/j.cej.2009.01.017.
[54] L. Xu, J. Wang, A heterogeneous Fenton-like system with nanoparticulate zero-valent iron for removal of 4-chloro-3-methyl phenol, J. Hazard. Mater. 186 (2011) 256–264, https://doi.org/10.1016/j.jhazmat.2010.10.116.
[55] J.H. Ramirez, F.J. Maldonado-Hódar, A.F. Pérez-Cadenas, C. Moreno-Castilla, C. A. Costa, L.M. Madeira, Azo-dye Orange II degradation by heterogeneous Fenton-like reaction using carbon-Fe catalysts, Appl. Catal. B: Environ. 75 (2007) 312–323, https://doi.org/10.1016/j.apcatb.2007.05.003.
[56] Q. Wang, B. Wang, Y. Ma, S. Xing, Enhanced superoxide radical production for ofloxacin removal via persulfate activation with Cu-Fe oxide, Chem. Eng. J. 354 (2018) 473–480, https://doi.org/10.1016/j.cej.2018.08.055.
[57] V.T. Le, V.A. Tran, D.L. Tran, T.L.H. Nguyen, V.D. Doan, Fabrication of Fe_3O_4/CuO@C composite from MOF-based materials as an efficient and magnetically separable photocatalyst for degradation of ciprofloxacin antibiotic, Chemosphere 270 (2021) 129417, https://doi.org/10.1016/j.chemosphere.2020.129417.
[58] L. Ai, C. Zhang, L. Li, J. Jiang, Iron terephthalate metal–organic framework: revealing the effective activation of hydrogen peroxide for the degradation of organic dye under visible light irradiation, Appl. Catal. B: Environ. 148–149 (2014) 191–200, https://doi.org/10.1016/j.apcatb.2013.10.056.
[59] C. Zhao, Z.H. Wang, X. Li, X.H. Yi, H.Y. Chu, X. Chen, C.C. Wang, Facile fabrication of BUC-21/$Bi_{24}O_{31}Br_{10}$ composites for enhanced photocatalytic Cr(VI) reduction under white light, Chem. Eng. J. 389 (2020) 123431, https://doi.org/10.1016/j.cej.2019.123431.
[60] J. Jiang, D.I. Kim, P. Dorji, S. Phuntsho, S. Hong, H.K. Shon, Phosphorus removal mechanisms from domestic wastewater by membrane capacitive deionization and system optimization for enhanced phosphate removal, Process Saf. Environ. 126 (2019) 44–52, https://doi.org/10.1016/j.psep.2019.04.005.
[61] M. Mahdi Ahmed, S. Barbati, P. Doumenq, S. Chiron, Sulfate radical anion oxidation of diclofenac and sulfamethoxazole for water decontamination, Chem. Eng. J. 197 (2012) 440–447, https://doi.org/10.1016/j.cej.2012.05.040.
[62] J. Jiang, X. Wang, Y.i. Liu, Y. Ma, T. Li, Y. Lin, T. Xie, S. Dong, Photo-Fenton degradation of emerging pollutants over Fe-POM nanoparticle/porous and ultrathin g-C_3N_4 nanosheet with rich nitrogen defect: degradation mechanism, pathways, and products toxicity assessment, Appl. Catal. B: Environ. 278 (2020) 119349, https://doi.org/10.1016/j.apcatb.2020.119349.
[63] C. Zhao, J.S. Wang, X. Chen, Z.H. Wang, H.D. Ji, L. Chen, W. Liu, C.C. Wang, Bifunctional $Bi_{12}O_{17}Cl_2$/MIL-100(Fe) composites toward photocatalytic Cr(VI) sequestration and activation of persulfate for bisphenol A degradation, Sci. Total Environ. 752 (2021) 141901, https://doi.org/10.1016/j.scitotenv.2020.141901.
[64] S.W. Lv, J.M. Liu, N. Zhao, C.Y. Li, Z.H. Wang, S. Wang, Benzothiadiazole functionalized Co-doped MIL-53-NH_2 with electron deficient units for enhanced photocatalytic degradation of bisphenol A and ofloxacin under visible light, J. Hazard. Mater. 387 (2020) 122011, https://doi.org/10.1016/j.jhazmat.2019.122011.
[65] Y.H. Li, X.H. Yi, Y.X. Li, C.C. Wang, P. Wang, C. Zhao, W. Zheng, Robust Cr(VI) reduction over hydroxyl modified UiO-66 photocatalyst constructed from mixed ligands: performances and mechanism insight with or without tartaric acid, Environ. Res. 201 (2021) 111596, https://doi.org/10.1016/j.envres.2021.111596.
[66] S. Guo, Z. Yang, H. Zhang, W. Yang, J. Li, K. Zhou, Enhanced photocatalytic degradation of organic contaminants over $CaFe_2O_4$ under visible LED light irradiation mediated by peroxymonosulfate, J. Mater. Sci. Technol. 62 (2021) 34–43, https://doi.org/10.1016/j.jmst.2020.05.057.
[67] Y. Guo, L. Yan, X. Li, T. Yan, W. Song, T. Hou, C. Tong, J. Mu, M. Xu, Goethite/biochar-activated peroxymonosulfate enhances tetracycline degradation: inherent roles of radical and non-radical processes, Sci. Total Environ. 783 (2021) 147102, https://doi.org/10.1016/j.scitotenv.2021.147102.
[68] F.-X. Wang, C.-C. Wang, X. Du, Y. Li, F. Wang, P. Wang, Efficient removal of emerging organic contaminants via photo-Fenton process over micron-sized Fe-MOF sheet, Chem. Eng. J. 429 (2022) 132495, https://doi.org/10.1016/j.cej.2021.132495.
[69] M. Jiang, J. Lu, Y. Ji, D. Kong, Bicarbonate-activated persulfate oxidation of acetaminophen, Water Res. 116 (2017) 324–331, https://doi.org/10.1016/j.watres.2017.03.043.
[70] F. Wang, H. Fu, F.X. Wang, X.W. Zhang, P. Wang, C. Zhao, C.C. Wang, Enhanced catalytic sulfamethoxazole degradation via peroxymonosulfate activation over amorphous CoSx@SiO_2 nanocages derived from ZIF-67, J. Hazard. Mater. 423 (2022) 126998, https://doi.org/10.1016/j.jhazmat.2021.126998.
[71] V.K. Sharma, M. Feng, Water depollution using metal-organic frameworks-catalyzed advanced oxidation processes: a review, J. Hazard. Mater. 372 (2019) 3–16, https://doi.org/10.1016/j.jhazmat.2017.09.043.
[72] B. Palanivel, M. Lallimathi, B. Arjunkumar, M. Shkir, T. Alshahrani, K.S. Al-Namshah, M.S. Hamdy, S. Shanavas, M. Venkatachalam, G. Ramalingam, rGO supported g-C_3N_4/$CoFe_2O_4$ heterojunction: visible-light-active photocatalyst for effective utilization of H_2O_2 to organic pollutant degradation and OH radicals production, J. Environ. Chem. Eng. 9 (1) (2021) 104698, https://doi.org/10.1016/j.jece.2020.104698.
[73] G. Liu, G. Zhao, W. Zhou, Y. Liu, H. Pang, H. Zhang, D. Hao, X. Meng, P. Li, T. Kako, J. Ye, In situ bond modulation of graphitic carbon nitride to construct p-n homojunctions for enhanced photocatalytic hydrogen production, Adv. Funct. Mater. 26 (2016) 6822–6829, https://doi.org/10.1002/adfm.201602779.
[74] S. Cao, B. Shen, T. Tong, J. Fu, J. Yu, 2D/2D heterojunction of ultrathin MXene/Bi_2WO_6 nanosheets for improved photocatalytic CO_2 reduction, Adv. Funct. Mater. 28 (21) (2018) 1800136, https://doi.org/10.1002/adfm.201800136.
[75] J. Liu, X. Zhang, Q. Zhong, J. Li, H. Wu, B. Zhang, L. Jin, H.B. Tao, B. Liu, Electrostatic self-assembly of a AgI/$Bi_2Ga_4O_9$ p–n junction photocatalyst for boosting superoxide radical generation, J. Mater. Chem. A 8 (2020) 4083–4090, https://doi.org/10.1039/c9ta13724f.
[76] J. Jinhui, L. Kuili, F. Weiqiang, L. Meng, L. Yu, M. Baodong, B. Hongye, S. Hongqiang, Y. Songliu, S. Weidong, Electrospinning synthesis and photocatalytic property of Fe_2O_3/$MgFe_2O_4$ heterostructure for photocatalytic degradation of tetracycline, Mater. Lett. 176 (2016) 1–4, https://doi.org/10.1016/j.matlet.2016.03.016.
[77] Y. Tian, N. Jia, H. Ma, G. Liu, Z. Xiao, Y. Wu, L. Zhou, J. Lei, L. Wang, Y. Liu, J. Zhang, 0D/3D coupling of g-C_3N_4 QDs/hierarchical macro-mesoporous CuO-SiO_2 for high-efficiency norfloxacin removal in photo-Fenton-like processes, J. Hazard. Mater. 419 (2021) 126359, https://doi.org/10.1016/j.jhazmat.2021.126359.